Journal of Research in Science and Engineering (JRSE)
ISSN: 1656-1996 Volume-8, Issue-3, March 2026
DOI: 10.53469/jrse.2026.08(03).19

Microwave Hydrothermal Synthesis of $NaNi_{1/3}Fe_{1/3}Mn_{1/3}O_2$ and Its Performance in Sodium Ion Batteries

Xueyan Dong

School of Chemistry and Materials Science, Qinghai Minzu University, Xi'ning 810007, China

Abstract: ***Global energy storage resources are facing shortages, while market demand continues to grow rapidly. The abundance of sodium resources and the low cost of sodium salts make sodium-ion batteries a promising candidate for large-scale energy storage applications. Among various cathode materials, layered transition metal oxides have attracted significant attention due to their structural advantages. However, these materials often suffer from transition metal layer sliding during sodium extraction and insertion, leading to limited capacity, poor phase transition stability, and restricted practical application. This study systematically investigates the application of microwave-assisted synthesis in the preparation of sodium-ion battery cathode materials. Through comparative experiments, the unique advantages of microwave-assisted synthesis in optimizing structure and performance are revealed. Focusing on the nickel-iron-manganese ternary layered oxide $NaNi_{1/3}Fe_{1/3}Mn_{1/3}O_2$ (NFM) as a cathode material for sodium-ion batteries, NFM prepared by microwave-assisted hydrothermal method was compared with that synthesized by conventional hydrothermal method. The results indicate that the microwave-assisted hydrothermal method produces NFM with superior microscopic morphological characteristics, more uniform grain size, and significantly improved geometric regularity of the hexagonal crystal structure. This material exhibits excellent electrochemical performance, with an initial discharge capacity of 96.24 mAh g^{-1} at 1C current density and a capacity retention of 88.67 mAh g^{-1} after 150 cycles. By adjusting the synthesis temperature and PH, the optimal conditions for microwave-assisted synthesis were determined to be 170°C and PH=10. The NFM material prepared under these conditions demonstrates high crystallinity, uniform nano-morphology, and excellent sodium-ion diffusion kinetics, achieving an initial discharge capacity of 100.4 mAh/g (1C), indicating strong application potential.***

1. Introduction

Currently, China's energy structure is dominated by coal, supplemented by fossil energy sources such as oil and natural gas, while the proportion of clean energy continues to increase, and the energy structure is transforming into a diversified and cleaner one. Under the synergistic effect of technological breakthroughs and policy support, the development potential of the energy sector will be further released, providing a strong impetus for the green low-carbon transformation [1]. Large-scale application of renewable energy is to reduce fossil energy pollution, promote the key path of low-carbon transformation, and efficient energy storage technology is to realize new energy stable grid and support the core support of the "dual carbon" strategic objectives [2] [3] [4]. In the context of energy security and ecological protection of the double constraints are increasingly prominent, electrochemical energy storage technology for the green change of the energy system provides an innovative solution.

Among them, lithium-ion batteries have become the most commercially valuable technology route in the field of electrochemical energy storage at present due to their significant advantages of high energy density, fast response speed, and strong geographic adaptability. However, as the market demand for lithium-ion batteries continues to expand, the problems of tight supply and price fluctuations of lithium resources are becoming more and more prominent. This has also forced many researchers to turn their attention to sodium, which is located in the same main group as lithium. Sodium-ion batteries instead of lithium-ion batteries have the advantages of abundant resources, low cost, environmentally friendly, high safety, and suitable for large-scale energy storage [5] [6] [7]. Its significance lies not only in alleviating the pressure of lithium resource shortage and energy shortage, but also in promoting the development of green energy technology, improving energy security and promoting the global energy transition. With the continuous progress of technology and accelerated industrialization, sodium-ion battery technology, due to its unique advantages, will become a key component of the future energy storage system, promoting clean energy transition and sustainable development [8] [9]. Sodium-ion batteries are slightly lower than lithium-ion batteries in terms of energy density, but sodium-ion batteries can be expected to be used in large-scale applications such as energy storage systems, low-speed electric vehicles, and 5G communication base stations by virtue of their abundant reserves of earth's elements as well as their low price [10] [11].

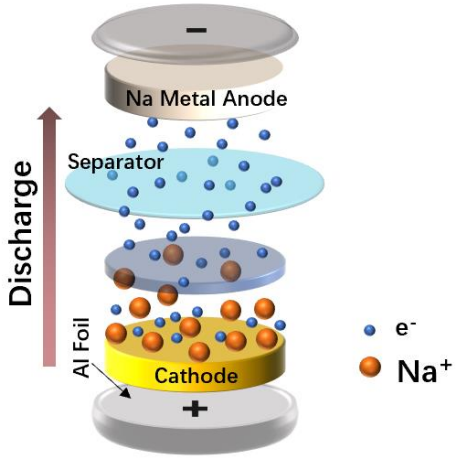

Figure 1: The composition of sodium ion battery and its ' rocking chair ' working principle

A secondary battery, also known as a rechargeable battery, is an electrochemical energy storage device that can be charged by an external power source and used multiple times. Figure 1

shows a schematic diagram of its working principle, and its internal structure includes the following key parts: positive electrode, negative electrode, electrolyte, diaphragm, and case. Sodium-ion batteries use a dual-collector system of aluminum (positive electrode) and copper (negative electrode). During charging, Na^+ is detached from the lattice of the positive material and diffuses to the negative electrode through the electrolyte; synchronously, electrons are transferred to the negative electrode through an external circuit thus realizing the conversion between electrical and chemical energy [12].

The chemical general formula of sodium base layer-like oxides is generally Na_xTMO_2, and their structures are mainly divided into P3, P2, O3, and O2 insertion of structural diagrams where P and O are the abbreviations of prismatic and octahedral, respectively, which indicate that the alkali metal layers of Na^+ are in a trigonal prismatic mode of occupation and an octahedral coordination environment, and the numbers 2 and 3 stand for the number of MO_2 layers in a single cell with different stacking modes (e.g., 2 for ABBA and 3 for ABCABC) [13]. Unlike lithium layered oxides, the P-type structure is also unique to sodium-ion layered oxides due to the larger radius of Na^+, which can be stabilized in the alkali-metal layer as a trigonal prism occupation [14]. Figure 2 shows the schematic structure of each phase of layered metal oxides [15].

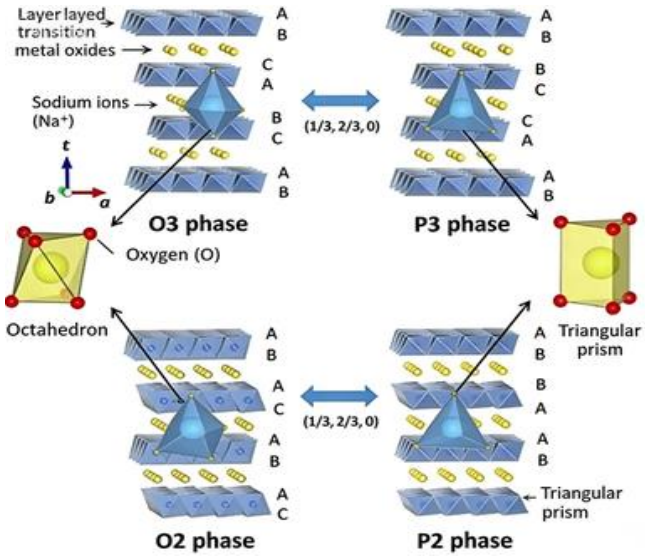

Figure 2: Schematic structure of each phase of layered metal oxides

Research on cathode materials for sodium-ion batteries has been initiated since the 1970s, and the early studies were faced with two key challenges: first, the susceptibility of layered oxides to structural collapse during charging and discharging (e.g., P2 O2 phase transition leading to a volume change of more than 10%), and second, the limited multiplicative performance due to the low intrinsic electrical conductivity of the materials (generally $<10^{-5}$S/cm) [16].

In the commercial Li-ion battery cathode material system, $LiCoO_2$, as the first industrialized layered oxide material (O3-type structure, space group R-3m), laid the foundation for subsequent development [17]. Similar to the lithium-ion layered oxide structure, sodium-ion layered oxides are considered to be the most promising cathode materials for commercialization. Sodium-ion layered oxide materials face two major key challenges in practical applications: first, due to the large ionic radius of Na^+(1.02 Å), its diffusion kinetics in the crystal structure is significantly limited, resulting in poor multiplicative performance of the electrode materials; second, during the repeated delocalization and embedding of Na^+, the crystal structure of the materials is susceptible to various forms of irreversible damage, including but not limited to 1) irreversible reversible phase transition; 2) Jahn-Teller lattice distortion; 3) transition metal ion migration; 4) lattice oxygen loss and other phenomena. These structural degradation mechanisms can severely damage the lamellar framework of the material, which in turn leads to a rapid degradation of the electrochemical properties [18] [19]. Na^+/vacancy ordered rearrangements are also believed to cause the formation of multiple intermediate transition phases, which reduces the Na^+ transport rate.

The author systematically reviews [20] the current applications of layered oxide cathode materials in sodium-ion batteries (SIBs), analyzing their three major challenges: poor air stability, interfacial instability, and irreversible phase transitions. Improvement strategies such as structural optimization, interface reconstruction, and chemical substitution are summarized. Methods including superlattice ordering, surface coating, and elemental doping effectively enhance material performance. Finally, future research directions are outlined, providing theoretical guidance for developing high-performance SIB cathode materials. Yao et al [15] investigated hexagonal lamellar Ni/Mn base layer oxide cathode materials with multi-element doping and ZrO_2 surface modification to enhance their application performance in performance in sodium-ion battery applications. The results showed that the synergistic effect of multi-element doping and ZrO_2 surface modification effectively enhanced the cycling stability and air stability of the materials. Prof. Ky Tae Lee and his team [21] investigated the electrochemical performance of P3-type $Na_{0.67}$ $[Li_{0.1}(Fe_{0.5}Mn_{0.5})_{0.9}]O_2$ and compared it with P2-type $Na_{0.67}$ $[Fe_{0.5}Mn_{0.5}]$ O_2 was compared. They found that Li^+ doping inhibits the migration of Fe^{3+} ions to tetrahedral sites, which significantly improves the cycling stability and multiplicity performance of the materials. Qin-Chao and his research team successfully enhanced the electrochemical performance of P2-$Na_{0.67}Mn_{0.67}Ni_{0.33}O_2$ through Sb^{5+} doping, which effectively modulated the Na-site occupancy and suppressed the detrimental P2-O2 phase transition. This innovative approach significantly improved the material's cycling stability and rate capability, offering a promising new strategy for the design of advanced cathode materials in sodium-ion batteries [22]. The team [23] led by Tengfei Song significantly improved the structural stability and electrochemical performance of O3-type Na $[Ni_{1/3}Fe_{1/3}Mn_{1/3}]O_2$ cathode materials through synergistic Sn doping and surface coating. The 8% Sn-doped sample exhibited a capacity retention rate of 70.07% after 150 cycles within 2.0-4.1 V, while suppressing phase transitions and interfacial side reactions, providing a new strategy for designing high-performance sodium-ion battery cathodes. Chenchen Wang et al [24] demonstrated that incorporating K^+ into P2-$Na_{0.612}K_{0.056}MnO_2$ effectively modulates the local chemical environment, significantly enhancing the performance of sodium-ion battery cathodes. The modified material delivers a high capacity of 240.5 mAh/g with excellent cycling stability, offering a novel design strategy for

SIBs cathode materials. R.A. Harindi Gayara's team [25] synthesized $Na_1Ni_{0.33}Mn_{0.33}Fe_{0.33}O_2$ via microwave-assisted sol-gel, showing enhanced structural/electrochemical stability over conventional sintering. Characterization confirmed superior thermal/cycling performance, advancing cost-effective Na-ion batteries. In recent years, microwave-assisted hydrothermal synthesis has shown significant advantages in the controlled synthesis of nanomaterials due to its unique rapid and uniform heating mechanism. Compared with the traditional hydrothermal method, microwaves can achieve efficient activation of reactants at the molecular scale through dielectric loss and dipole polarization, thus precisely regulating the crystallinity, morphology and interfacial properties of materials [26] [27] [28] [29] [30] [31].

In this study, a series of $NaNi_{1/3}Mn_{1/3}Co_{1/3}O_2$ ternary cathode materials with tunable synthesis parameters were prepared via microwave-assisted hydrothermal method. The systematic investigation focused on the influence of microwave temperature and irradiation conditions on the material's crystal structure, morphological characteristics, and sodium storage performance. The microwave-assisted synthesis approach was found to facilitate the formation of homogeneous structures with abundant active sites, enhanced ionic diffusion kinetics, and superior structural stability, leading to significantly improved electrochemical performance in sodium-ion batteries. Furthermore, detailed analysis of pseudocapacitive contributions and reaction kinetics provided mechanistic insights into the excellent electrochemical properties of these electrode materials.

2. Experimental

2.1 Materials Preparation

All of the following chemical reagents are analytical pure

2.2 Preparation of $Ni_{1/3}Fe_{1/3}Mn_{1/3}(OH)_2$ Precursors

Manganese acetate, nickel acetate and ferrous sulfate hydrate were selected as manganese source, nickel source and iron source for the experiments; equal proportions of manganese source, nickel source and iron source were weighed and dissolved in 20 ml of deionized water as solution A. The solution was stirred and dissolved well with a magnetic stirrer at a rotational speed of 300 rpm, and the appropriate amount of sodium hydroxide and polyethylene glycol were dissolved in 20 ml of deionized water as solution B. The fully dissolved solution B was slowly poured into solution A at a drop rate of 1 ml/min. dissolved solution B was slowly poured into solution A at a drop rate of 1 ml/min. And at the same stirring rate, stirred for 30 min to make it mixed uniformly; ammonia was used to adjust the PH of the solution to 9, 10, 11, respectively, and continued to be stirred for 30 min on a magnetic stirrer, then the mixed uniform solution was transferred to a polytetrafluoroethylene-lined high-pressure reactor for a hydrothermal reaction; or the solution was poured into a microwave hydrothermal reaction apparatus for the reaction in this step. The microwave reactor was set to 600 W, the reaction time was 30 min, the temperature increase rate was 3 ℃/min, and the holding time was 5 min for each stage, based on which the temperature was set to 160 ℃, 170 ℃, 180 ℃, respectively, and then the solutions obtained from hydrothermal and microwave hydrothermal were transferred to centrifuge tubes and separated by centrifugation at 8000 rpm for 5 min. The ternary precursor $Ni_{1/3}Fe_{1/3}Mn_{1/3}(OH)_2$ was washed several times with deionized water and anhydrous ethanol, and then dried in a vacuum oven at 80 ℃ for 12 h. The ternary precursor $Ni_{1/3}Fe_{1/3}Mn_{1/3}(OH)_2$ could be obtained by grinding uniformly.

2.3 Preparation of $NaNi_{1/3}Fe_{1/3}Mn_{1/3}O_2$ (NFM)

The prepared ternary precursor material $Ni_{1/3}Fe_{1/3}Mn_{1/3}(OH)_2$ was fully mixed and ground with anhydrous sodium carbonate in equal proportions, in which the anhydrous sodium carbonate should be 5% overdose, and after mixing evenly, it was transferred to a muffle furnace, and then roasted at 500 ℃ under air atmosphere for 5 h and then 800 ℃ under the temperature rise rate of 5 ℃/min for 8 h. The sintered samples were crushed and then the $NaNi_{1/3}Fe_{1/3}Mn_{1/3}O_2$ (NFM) pristine material was obtained. $NaNi_{1/3}Fe_{1/3}Mn_{1/3}O_2$ (NFM) pristine material.

The NFM obtained by hydrothermal, microwave-assisted were noted as S-NFM, W-NFM, respectively.

The NFM obtained by adjusting the temperature and PH were noted as W-160 ℃-NFM, W-170 ℃-NFM, W-180 ℃-NFM, W-180 ℃-PH=9-NFM, W-180 ℃-PH=11-NFM, respectively.

2.4 Materials Characterization

X-ray powder diffraction (XRD) was recorded using Cu Kα (λ = 1.5418 Å) on Ultima IV.

Morphological features of the samples were observed by Thermo Fisher Scientific Apreo C field emission electron microscopy (SEM).

The microstructure and lattice striations were observed by Jem-2100F transmission electron microscope (TEM).

Adsorption-desorption isotherms were tested on a KuboX1000 specific surface area analyzer. Specific surface area was calculated by BET method. Barrett-Joyner-Halenda model was used to derive the pore size distribution of the desorption branch.

X-ray photoelectron spectroscopy (XPS) tests were performed on a Thermo Fisher Nexsa photoelectron spectroscopy instrument.

2.5 Electrochemical Characterization

The active material, acetylene black, and polytetrafluoroethylene (PVDF) were mixed in N-methylpyrrolidone (NMP) at a weight ratio of 8:1:1 to form a homogeneous slurry, which was then uniformly coated on aluminum foil. The area of active material on each electrode was 1.13 cm2 with a mass loading of ~1.5 mg/cm2. The cells were packed in a glove box with H2O < 0.1 ppm and O2 < 0.1 ppm. The electrolyte was 1 mol/L NaClO4 (1:1:1, 5% FEC by volume) dissolved in EC, DEC, and EMC. Sodium metal was

used as the negative electrode and glass fiber membrane Whatman GF/A was used as the diaphragm. Constant-current charge/discharge tests were performed on a Sunway battery test system (CT-4008-5V10mA) with a voltage range of 2.5-4.0 V (Na^+/Na).CV and EIS tests were performed on a Chenhua electrochemical workstation (CHI760E). The EIS tests were performed in the frequency range of 0.01 Hz-105 Hz with an amplitude of 5 mV/s. The EIS tests were performed at a frequency of 1.5 V (Na^+/Na).

3. Results and Discussion

3.1 Morphology and Structure Characterization

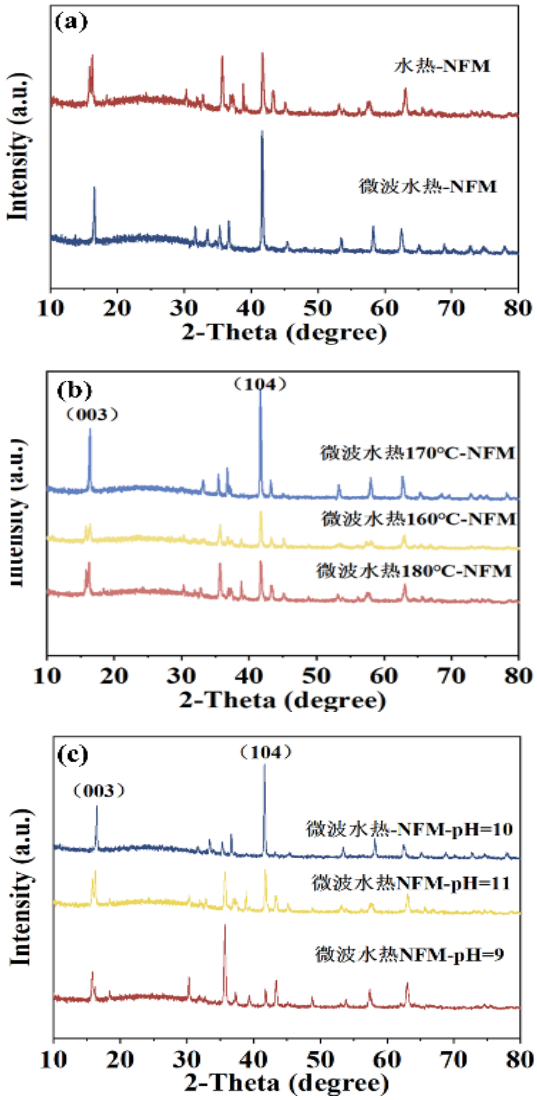

Figure 3: XRD of NFM samples synthesized under different preparation conditions

Typical ternary material $NaNi_{1/3}Fe_{1/3}Mn_{1/3}O_2$ (NFM) has been prepared by hydrothermal as well as microwave hydrothermal methods, and as can be seen in Figure 3 (a), the samples obtained by the two synthesized methods exhibit different diffraction peaks on the XRD patterns, which indicates the differences in their crystal structures or phase compositions. In addition, by comparing these two materials, we can see that the NFM material prepared by microwave hydrothermal is more crystalline than the NFM material prepared by hydrothermal method.

Figure 3(b) shows the X-ray diffraction (XRD) patterns of the samples after microwave hydrothermal treatment at three different temperatures. By comparison, the changes in the crystal structure of the samples after treatment at different temperatures can be observed. It can be seen that the NFM materials with different synthesis temperatures have the same diffraction peaks, which indicates that the crystal structure has not been changed. Comparing the (003) diffraction peak and the (104) diffraction peak labeled in the figure, it can be seen that the NFM prepared by microwave hydrothermal at 170 ℃ has sharper diffraction peaks, higher crystallinity and higher phase purity [32].

The X-ray diffraction (XRD) patterns of the samples after microwave hydrothermal treatment at three different PH values are illustrated in Figure 3(c). samples at PH 10 and 11 have distinct diffraction peaks at the same 2Θ angles (about 15° and 40°), corresponding to the (003) and (104) crystalline planes, respectively. This indicates that the crystal structures of NFM are basically similar at these PH conditions, and also indicates that the lattice parameters are not significantly changed at different PH conditions. However, the diffraction peaks of the material at PH=9 are different from those of the other two materials, which may be due to the fact that the material was not successfully synthesized at PH=9, while the stronger diffraction peaks indicate that the atomic arrangement of this crystal face is more ordered. The XRD analysis results show that the resulting materials exhibit the best crystallinity and PHase purity when the PH of the synthesized system is 10, which confirms that this PH condition is the optimal synthesis parameter.

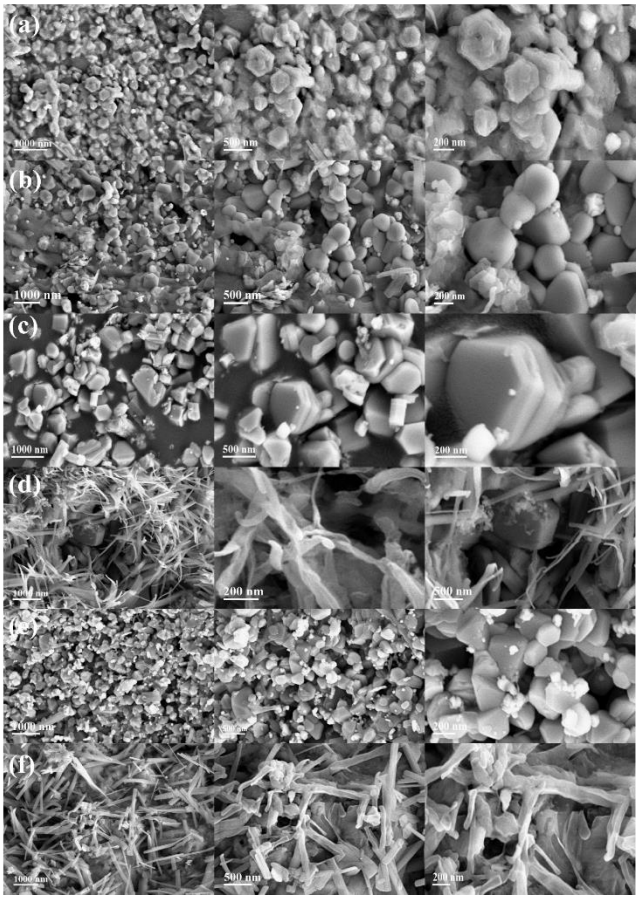

Figure 4: (a-f) SEM images of NFM samples prepared under microwave hydrothermal 180 ℃, PH=10; (d-f) SEM images of NFM samples prepared under hydrothermal 180 ℃, PH=10

Figure 4(a) shows the NFM samples prepared under microwave hydrothermal 180 ℃, PH=10, which shows that the material exhibits an obvious hexahedral morhphology, with a grain size range of 50-200 nm. Figure 4(b) shows the NFM samples prepared under hydrothermal 180 ℃, PH=10, which shows that the material exhibits nanosheets and fibers morphology, however, there is an obvious agglomeration between the material particles phenomenon and the range of grain size is not clear. By comparing the overall morphology of the material with the particle size in Figure 4(a-b), it can be seen that the particle distribution of the material prepared by microwave hydrothermal is more uniform under the same PH condition. However, it is worth noting that the nanosheets as well as the fiber structure shown in Figure 4 may be due to the formation of the material during the preparation process. The comparison shows that microwave-assisted synthesis helps to form materials with uniform size and high crystallinity.

The SEM images of Figure 4(c-d) show the nanomorphology of microwave solvent-heated NFM powders under the synthesis conditions of different temperatures at the same PH value, of which Figure 4(c) is the NFM sample prepared under microwave solvent-heating at 160 ℃ and PH=10, which shows that the material exhibits a clear hexahedral morphology, with irregular shaped particles, larger particles, uneven distribution, and a range of grain sizes from 50-400 nm. Figure 4(d) shows the NFM samples prepared under microwave solvent heating at 170 ℃ and PH=10, which shows that the material exhibits a hexahedral morphology, with the grain size ranging from 100-400 nm, which may be due to the agglomeration phenomenon of the material. Compared with the material at a temperature of 180 ℃, something agglomerates and solidifies in the surface layer of the material at a temperature of 160 ℃. And when the temperature is 170 ℃, the individual grains of the material are destroyed, although its XRD pattern shows a better crystallinity of the material, but in the SEM, the material is destroyed. It should be that the temperature deviation from the optimal range leads to the imbalance of crystal growth kinetics, i.e., the reactants are not active enough at low temperatures, and the anisotropic growth is hindered; while the high temperature triggers the convergence of crystalline energy, which leads to the overgrowth of the thermodynamically stable nonpolar crystalline surfaces, and destroys the hexahedral morphology.

Through the comparative study of the microstructure of the three materials, it is found that they have similar morphology characteristics, but the change of grain size with the synthesis temperature shows an obvious law: with the increase of temperature, the material grain size gradually decreases. When the temperature reaches 180 ℃, the grain size of the resulting material is smaller and more uniformly distributed [33] [34].

Figure 4 (e) NFM samples prepared under microwave hydrothermal 180 ℃ and PH=11, it can be seen that the material shows nanowire-like shape, and the grains do not have an obvious size range. Compared to the materials with PH 9 and 10, the structure of the materials was destroyed at PH 11. Secondly, by comparing the grain size of the material at PH 9 and 10, it can be seen that at PH 10, the material particles are more uniformly distributed and smaller in size. And it is seen that at PH 11, the material is corroded and agglomerated. This is also consistent with the information from the XRD graph.

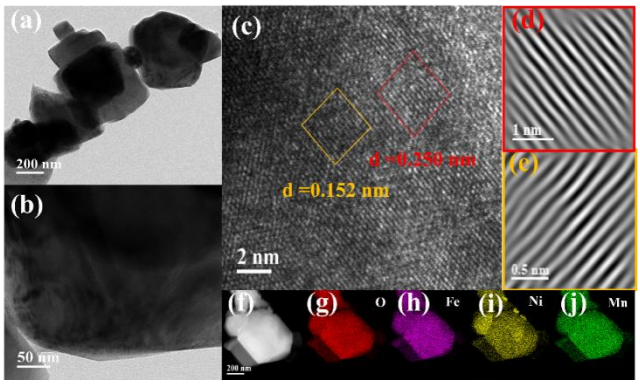

Figure 5: (a-b) W-180 ℃-PH=10-NFM transmission electron microscope (TEM); HRTEM of (c-e) W-180 ℃-PH=10-NFM; (f-j) element distribution diagram of W-180 ℃-PH=10-NFM;

According to the above SEM results, in order to further characterize the morphology lattice spacing of the ternary NFM cathode material, TEM tests were carried out on the NFM, as shown in Figure 5(a-e), from which it can be seen that the cathode material is in nano-hexahedral morPHology.5(a) is the high-resolution transmission electron microscope image of the ternary NFM, which shows the clear lattice stripes of the NFM, which indicates that the material is better crystallized, and the result is in agreement with the XRD This result is consistent with the XRD results.

The face-to-face spacing of neighboring lattice stripes in the TEM image is 0.250 nm, which is in good agreement with the spacing value of (003), and the face-to-face spacing of neighboring lattice stripes is 0.152 nm, which is in good agreement with the spacing value of (104). Whereas, in Figure 5 (f-j), it is observed that the elements Ni, Mn, Fe and O are uniformly distributed in the sample.

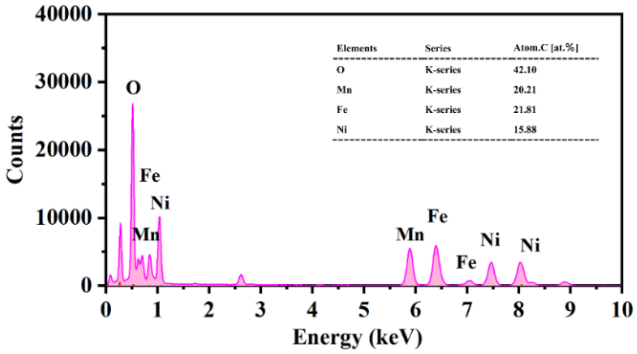

Figure 6: The EDS energy spectrum of NFM samples prepared at 180 ℃ and PH=10 by microwave hydrothermal method

And the corresponding energy spectra, it can be found that the three elements, Ni, Mn and Fe, are not synthesized according to the preparation of the ideal ratio of 1:1:1 ratio of the material, but slightly different from the ideal ratio. The ratio of the three elements Ni, Mn, and Fe in the material is approximated to be 1.2727:1.3734:1. However, the measured number of Fe atoms in the material is low due to the bias of EDS scanning due to region selection.

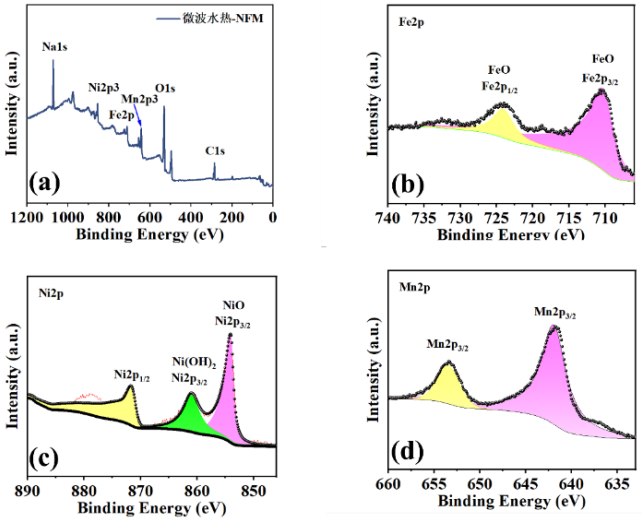

Figure 7: The XPS total spectrum and the fine spectra of Ni 2p, Mn 2p and Fe 2p of NFM prepared by microwave hydrothermal method

According to Figure 7, which shows the XPS of NFM prepared by microwave hydrothermal, the surface composition and valence states of the elements in the sample were analyzed by X-ray photoelectron spectroscopy (XPS). The full spectrum of XPS confirms the presence of the elements C, O, Fe, Mn, Ni, and Na in the sample, which is in agreement with the results of the EDS. The analysis of the fine spectrum of XPS shows that the Fe2p spectra at the binding energies of 724.0 eV and 710.4 eV show two distinct characteristic peaks corresponding to Fe2p1/2 (Fe-O bonding) and Fe2p3/2 (Fe-O bonding) electronic states, respectively. The Mn2p spectrum shows two distinct peaks at binding energies of 653.4 eV (Mn2p3/2) and 641.7 eV (Mn2p3/2), confirming the presence of the Mn element. 871.7 eV (Ni2p1/2), 860.8 eV (Ni2p3/2, corresponding to $Ni(OH)_2$ and 854.0 eV (Ni2p3/2, corresponding to NiO), which clearly reveal the chemical state of the Ni element and its oxides/hydroxides forms. and centered at 653.4 eV and a peak at 653.4 eV at higher binding energies were attributed to Mn^{3+} [35] [36]. The [37] O 1s spectrum shown inconfirms the metal-oxygen bonding from the peak at 529.5 eV. The above results confirm the chemical state of the elements on the surface of the material and their forms of existence, confirming the successful preparation of NFM nano-hexahedra.

3.2 Electrochemical Performance

The correct and successful synthesis of the material was confirmed by structural, morphological and elemental analyses, and the advantages of the microwave-assisted synthesis were analyzed in terms of the structure and morphology of the physical phases, as well as the determination of the optimal temperature and PH for the synthesis of the material. The XRD confirms that the material always maintains the O3 structure at PH values of 10 and 11. The SEM results confirm the optimal synthesis conditions, and the TEM high-resolution results clarify the lattice spacing of the material, which can be used to further identify the material as an O3 NFM, while the EDS results confirm the uniform elemental distribution of the material. The optimum synthesis conditions are derived from the micro-morphology of the material by comparison of microwave solvent heat and solvent heat, different temperatures and different PH values, which are verified by electrochemical test results.

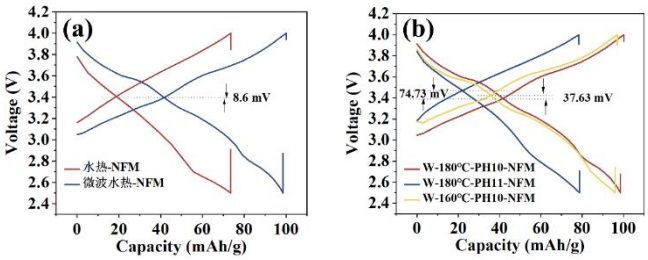

Figure 8: First charging and discharging of NFM samples synthesized by microwave hydrothermal under different conditions

Figure 8(a) shows the first-turn charge-discharge curves of NFM materials prepared by microwave solvent heating and solvent heating at 25 °C and 1 C. The first-turn charge-discharge curves of NFM materials prepared by microwave solvent heating and solvent heating are shown in Figure 8(b). By comparing these two groups, the charging and discharging plateaus of the materials prepared by both approaches are about 3.4 V, the voltage difference between the two is 8.6 mV, and the first charging specific capacities are 100.4 mAh/g and 73.8 mAh/g, and the first discharging specific capacities are 98.2 mAh/g and 72.8 mAh/g. The Coulombic efficiencies are 97.81% and 98.64%, respectively. The experimental results show that the ternary NFM nanomaterials prepared by microwave solvothermal method exhibit significant electrochemical performance advantages: 1) the first charge-discharge specific capacity is significantly improved compared with the traditional synthesized materials; 2) the charge-discharge curves do not show obvious polarization phenomenon at 1C multiplicity, especially the microwave-assisted synthesized samples have the smallest polarization voltage, and this feature fully proves that the materials prepared by this method have excellent cycling stability. These advantages are mainly attributed to the effective regulation of the crystal structure and morphology of the materials by microwave synthesis technology.

Figure 8(b) shows the first-cycle charge-discharge curves of NFM materials prepared under different conditions of microwave solvent heating at 25 °C and 1 C. The first-cycle charge-discharge curves of NFM materials prepared under different conditions of microwave solvent heating are shown in Figure 8(c). By comparing these three cases, the charge-discharge plateaus of the materials prepared under different conditions are all around 3.4 V. The voltage difference between microwave solvent heat 180 ℃ and microwave solvent heat 160 ℃, both of which are 37.63 mV, and the voltage difference between microwave solvent heat 180 ℃ and PH=10 and microwave solvent heat 180 ℃ and PH=11, both of which are 74.73 mV, and the specific capacity of the first charging are respectively 100.1 mAh/g, 97.1 mAh/g, 78.4 mAh/g, and the first discharge specific capacities were 98.5 mAh/g, 95.9 mAh/g, 78.1 mAh/g. The capacity retention rates were 98.40%, 98.76%, and 99.62%, respectively. The experimental results comparing the three preparation processes showed that the NFM nanomaterials synthesized under the optimized conditions of microwave solvothermal method at 180 °C and PH=10 exhibited the most excellent electrochemical properties. The charging and discharging curve plateau are the smoothest and the

polarization phenomenon is the least obvious. These results fully demonstrate that NFM cathode materials with outstanding cycling stability can be prepared by microwave solvothermal method under the specific conditions of 180 °C and PH=10.

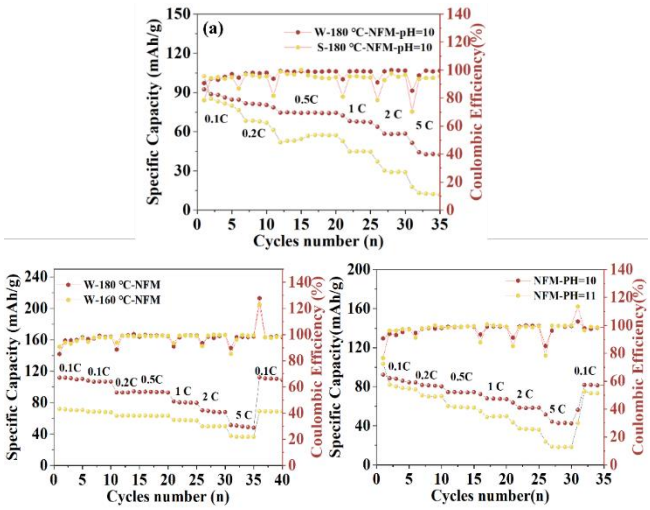

Figure 9: Rate test of NFM samples synthesized by microwave hydrothermal and hydrothermal methods

Figure 9(a) shows the multiplicity performance of microwave hydrothermal and hydrothermal prepared NFM materials at 25 °C, 0.1 C, 0.2 C, 0.5 C, 1 C, 2 C, 5 C, 0.1 C. From the above figure, it can be seen that the discharge specific capacity of solvent-heated synthesized NFMs at 1 C and 5 C is 57.12 mAh/g and 31.12 mAh/g, respectively, and that of the microwave solvent-heated synthesized NFMs is 71.20 mAh/g and 60.30 mAh/g, respectively. 71.20 mAh/g, 60.30 mAh/g, it can be seen that the discharge specific capacity of the microwave-assisted solvent-thermal synthesized material is much better than that of the material without microwave-assisted synthesis, no matter it is a high or a low magnification.

Figure 9(b) shows the multiplicity performance of NFM materials prepared by microwave solvent heat at different temperatures at 25 ℃, 0.1 C, 0.2 C, 0.5 C, 1 C, 2 C, 5 C, and 0.1 C. It can be seen from the figure that the discharge specific capacity of NFM synthesized by microwave solvent heat at 180 ℃ at 1 C and 5 C is 80.93 mAh/g and 53.01 mAh/g, respectively, and that the specific capacity of NFM synthesized by microwave solvent heat at 160 ℃ is 80.93 mAh/g and 53.01 mAh/g, respectively. NFM synthesized by microwave solvent heat at 160 ℃ had discharge specific capacities of 58.45 mAh/g and 35.90 mAh/g, respectively. The experimental data showed that the NFM material synthesized by microwave solvent heat at 180 ℃ (W-180 ℃-NFM) exhibited a better discharge specific capacity performance than the NFM material synthesized by microwave solvent heat at 160 ℃ (W-160 ℃-NFM) in different charging and discharging multiplicities. Performance. After several rounds of multiplicative cycling tests, W-180 °C-NFM and W-160 °C-NFM maintained 98.05% and 96.48% of the initial capacity, respectively, when the current density was brought back to 0.1 C, showing good electrochemical reversibility. This result is consistent with the above XRD, SEM, and first charge/discharge performance analysis.

Figure 9(c) shows the plots of multiplicity performance of NFM materials prepared at different PH values at microwave solvent heat 180 ℃ at 25 ℃, 0.1 C, 0.2 C, 0.5 C, 1 C, 2 C, 5 C and 0.1 C. The results are summarized in Figure 9(c). As can be seen from the graPHs, the discharge specific capacities of NFM synthesized by microwave solvent heat PH=10 at 1 C and 5 C are 48.96 mAh/g and 36.37 mAh/g, respectively, and those synthesized by microwave solvent heat PH=11 are 38.63 mAh/g and 17.06 mAh/g, respectively. The experimental data show that, at different charging and discharging multiplicity, NFM synthesized by microwave solvent heat PH=10 is the best choice to be used at different charge and discharge multiplicity rates. The experimental data show that, at different charge/discharge multiplication rates, the NFM materials synthesized by microwave solvent heating (W-NFM-PH=10) exhibit better discharge specific capacity performance than the PH=11 sample (W-NFM-PH=11). After several rounds of multiplicative cycling tests, W-NFM-PH=10 and W-NFM-PH=11 maintained 98.18% and 96.16% of the initial capacity, respectively, when the current density was brought back to 0.1 C, showing good electrochemical reversibility. This result is consistent with the above XRD, SEM, and first charge/discharge performance analysis.

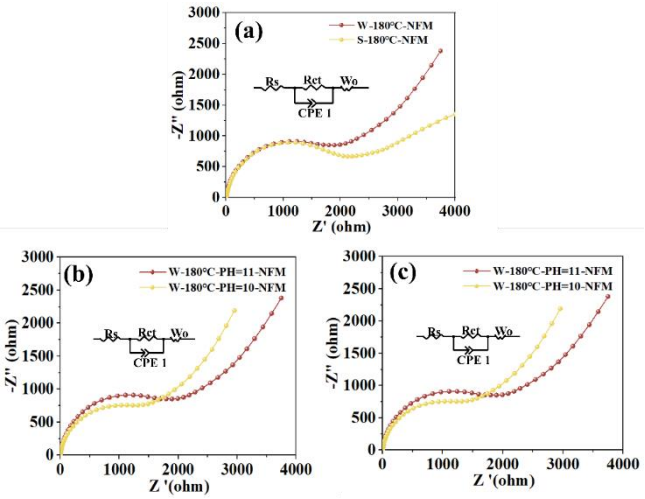

Figure 10: The equivalent circuit and EIS diagram of NFM samples synthesized by microwave hydrothermal and hydrothermal methods

Figure 10(a) shows the AC impedance (EIS) test of microwave solvent-heated and solvent-heated synthesized NFM samples after the activation of the completed battery, respectively, with a frequency range of 1 MHz to 0.01 Hz and an amplitude of 10 mV. Since the SOC has a large impact on the impedance of the battery, the NFM samples were uniformly charged to the fully charged state at constant current (SOC=100%) and left to stand for 30 min prior to the test to ensure the same testing state and the accuracy of the data. to ensure the same test state and data accuracy. A typical Nyquist diagram consists of two characteristic regions: the semicircular arc in the middle and high frequency regions corresponds to the charge transfer resistance (Rct), which reflects the charge transfer impedance at the electrode/electrolyte interface; the slash in the low frequency region represents the Warburg impedance (Wo), which characterizes the solid-PHase diffusion behavior of Na^+ in the electrode material.

Notably, the NFM materials synthesized by microwave solvothermal method exhibited lower resistance values than conventional solvothermal method in both impedance regions, as evidenced by smaller charge transfer resistance (Rct), indicating superior interfacial charge transfer kinetics, and lower Warburg impedance (Wo) reflecting faster Na^+ diffusion rate.

Figure 10(b) shows the AC impedance (EIS) test of the synthesized NFM samples under different conditions respectively in the cell after the activation was completed. Notably, the NFM materials synthesized by microwave solvothermal method at 180 °C and PH=10 exhibit lower resistance values in both impedance regions than the conventional solvothermal method, which are characterized by smaller charge transfer resistance (Rct), indicating superior interfacial charge transfer kinetics, and lower Warburg impedance (Wo) reflecting a faster Na^+ diffusion rate. This impedance property coincides with the crystal structural integrity shown by XRD and the favorable morPHological features observed by SEM, explaining the lower internal resistance as well as the superior electrochemical properties of the synthesized materials under optimal synthesis conditions.

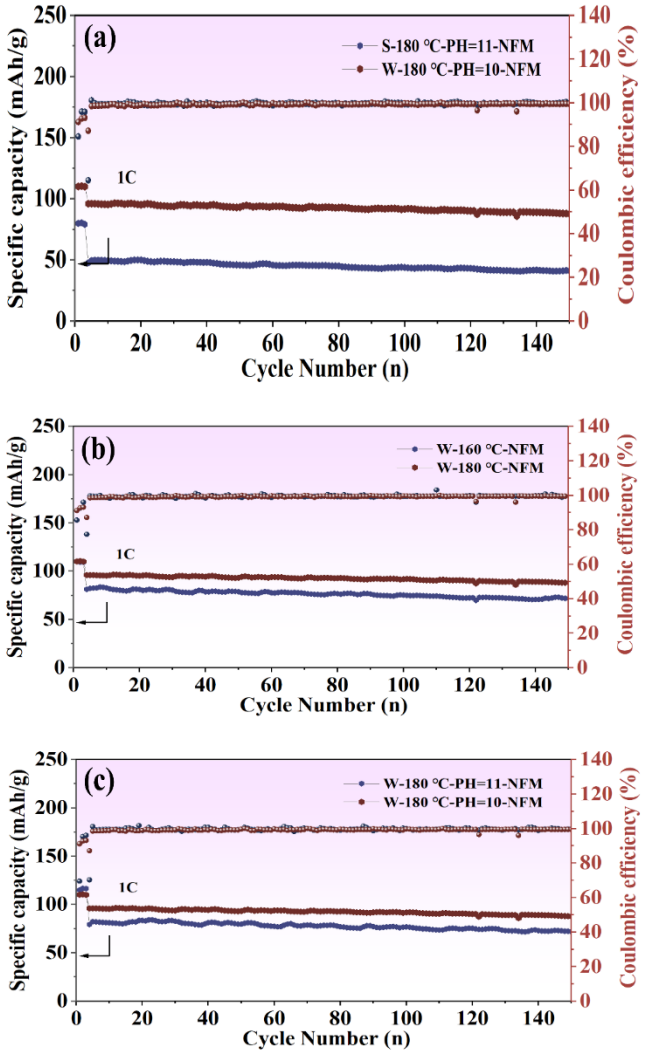

Figure 11: The cycle diagram of NFM materials prepared by hydrothermal and microwave hydrothermal methods

Figure 11(a) shows the cyclic diagrams of NFM materials prepared by hydrothermal and microwave hydrothermal, in the cyclic diagrams the initial discharge capacity of W-NFM is 100.41 mAh/g and that of S-NFM is 80.18 mAh/g. After three cycles of activation, the discharge specific capacities of both are 96.24 mAh/g and 50.92 mAh/g, and after 150 cycles the capacity After 150 cycles, the capacities decreased to 88.67 mAh/g and 41.45 mAh/g, respectively, and the capacity retention rates were 90.52% and 81.40%, respectively. Comparing the two, it can be concluded that the microwave-assisted preparation of the material has excellent cycling stability in the cycle, which is closely related to the better crystallinity and smaller particle size of the material.

Figure 11(b-c) shows the cycling diagrams of the NFM materials prepared under different conditions, in which the discharge capacities of W-180 ℃-NFM and W-160 ℃-NFM were 96.59 mAh/g and 80.52 mAh/g after three cycles of activation, and the capacities decreased to 88.66 mAh/g and 73.86 mAh/g after 150 cycles, and the capacity retention was 91.79% and 91.86%, respectively. were 91.79% and 91.72%. Comparing the two, it can be concluded that the material has a higher discharge specific capacity at 180 ℃, and its capacity retention rate is also better than that at 160 ℃. This also corresponds to the SEM and other tests of the material.

The initial discharge capacity of W-180 ℃-NFM-PH=10 and W-180 ℃-NFM-PH=11 in Cyclic Figure 12 was 100.41 mAh/g, and the initial discharge capacity of W-180 ℃-NFM-PH=11 was 116.37 mAh/g, and the discharge specific capacities of both were 96.59 mAh/g and 79.26 mAh/g after three turns of activation, and after 150 cycles, the After 150 cycles, the capacity decreased to 88.67 mAh/g and 70.07 mAh/g. The capacity retention rate was 91.80% and 88.40%, respectively. Comparing the two, it can be concluded that the material has a higher discharge specific capacity at temperature PH=10 and its capacity retention is also better than that of PH=11. By comparing the above two types of conditions, it can be concluded that the electrochemical performance of the material is more excellent when the microwave hydrothermal 180 ℃ and PH=10. This is mainly attributed to its uniform particle size and enhanced kinetic properties. As the particle size decreases, the NFM exposes more reactive sites, which makes the material have a higher capacity.

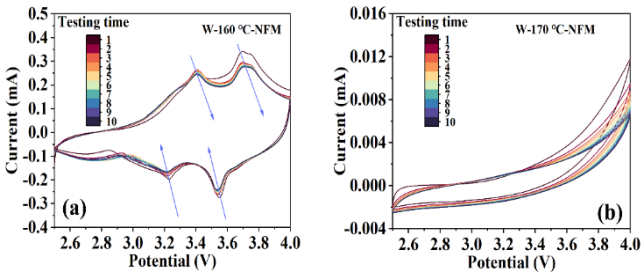

Figure 12: Cyclic voltammograms (CV) of NFM samples synthesized under different microwave hydrothermal conditions

Figure 12 shows the cyclic voltammograms (CV) of NFM materials prepared by microwave solvent heating at 160 ℃, PH=10 and 170 ℃, PH=10, with a scanning speed of 1 mV/s and a scanning range between 2.5-4.0 V. The CVs of NFM samples prepared by microwave solvent heating at 160 ℃, PH=10 are shown in Figure 12. From the figure, it can be seen that the samples prepared by microwave solvent heating 160 ℃, PH=10 show two pairs of redox peaks, and with the

increase of the scanning speed, it gradually tends to stabilize. The redox peak potentials of the NFM samples in the first loop of the cycle are 3.21 V/3.40 V and 3.53 V/3.69 V, respectively, and this corresponds to the corresponding this is also echoed with the results of the XRD and SEM tests. The sample prepared by microwave solvent heating at 170 °C and PH=10 shows only a pair of redox peaks, which are different from the CV of the other two materials with different temperatures and tend to stabilize gradually with the increase of scanning speed. This phenomenon may be due to the solid solution phase formation and the overlapping of Ni^{2+}/Ni^{4+} and Mn^{3+}/Mn^{4+} redox pair potentials in the NFM layered oxides, which resulted in the CV peaks merging.

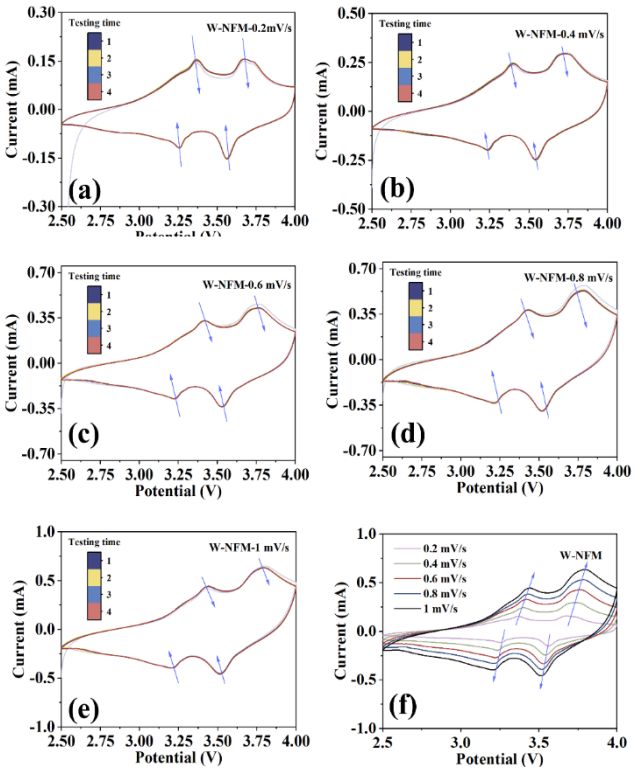

Figure 13: Cyclic voltammograms (CV) of NFM samples synthesized under microwave hydrothermal conditions

Figure 13 shows the cyclic voltammograms (CV) of NFM materials prepared under microwave solvent heating at 180 °C and PH=10 with scanning speeds of 0.2 mV/s, 0.4 mV/s, 0.6 mV/s, 0.8 mV/s, and 1 mV/s, and the scanning range was between 2.5-4 V. The NFM materials were activated by the microwave solvent heating at 0.2 mV/s. The material was subjected to a scan of 0.2 mV/s before a 10-turn scan was performed at a scan rate of 1 mV/s for activation. From the figure, it can be seen that the samples all show two pairs of redox peaks, and the area of the redox peaks is gradually expanding with the increase of the scanning speed. The redox peak potentials of the NFM samples at the first turn of the cycle are 3.43 V/3.19 V and 3.80 V/3.50 V, respectively, which corresponds to the Ni^{2+}/Ni^{4+} redox pairs, i.e., the phase transition of O3-P3. And the corresponding potential difference $\Delta\varphi$ between the anodic peak and the cathodic peak is 0.24 V and 0.3 V. It shows that at this time, the potential difference is small and the reversibility performance is better using the W-180 ℃-PH=10-NFM material.

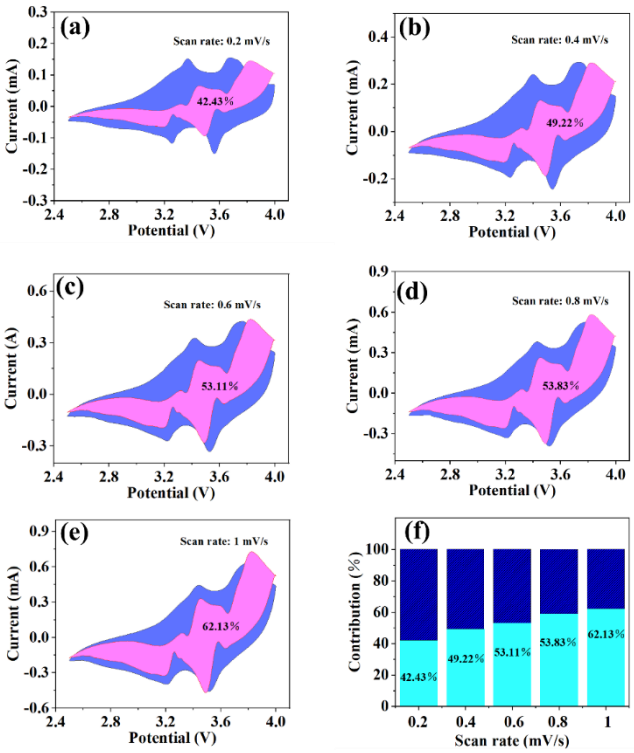

Figure 14: The diffusion control ratio of NFM at different scanning speeds, and the ratio of diffusion control to capacitance control of W-180 ℃-10-NFM samples at different scanning speeds.

Figure 15 depicts the ratio of capacitive and diffusive contributions for W-180 °C- PH=10-NFM samples at 0.2 mV/s, 0.4 mV/s, 0.6 mV/s, 0.8 mV/s, and 1 mV/s. The ratio of capacitive and diffusive contributions for the NFM samples is shown in Figure 14. and the ratio of diffusion control to capacitance control for NFM samples at different scanning speeds. It is noteworthy that even at 1.0 mV/s, the diffusive contribution still dominates with 62.13%. This shows that NFM favors the fastest diffusion kinetics of sodium ions due to its ultra-small particle size that shortens the diffusion path. These CV results verify that reducing the particle size is very favorable to improve the ion transport properties of the material.

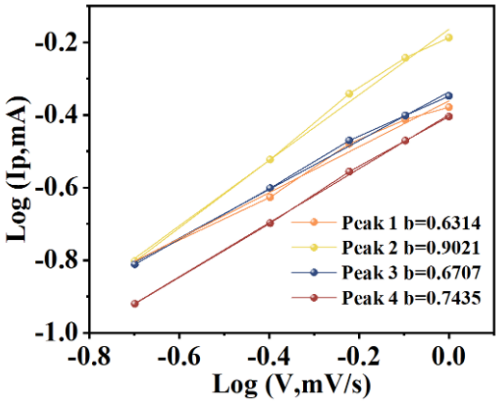

Figure 15: Linear fitting between log (IP) and log (V) of W-180 ℃-10-NFM samples

Figure 15 shows the linear fit between log (IP) and log(v) for

the W-180 °C- PH=10-NFM material, which is commonly used in electrochemical tests to analyze the charge storage mechanism of electrode materials, especially to distinguish between capacitive and diffusion-controlled behaviors.

Since the slope b is between 0.5 and 1, it suggests that the electrode reaction involves both diffusion control and capacitive behavior, i.e., the charge storage mechanism is hybrid, with the combined influence of diffusion and surface processes.

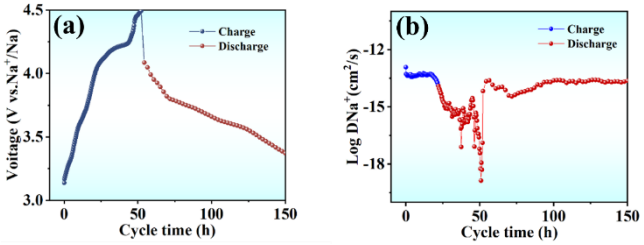

Figure 16: GITT test of microwave-assisted solvothermal W-180 °C- PH=10-NFM

Figure 16 depicts the GITT test at 0.05 C for the W-180 °C-PH=10-NFM sample. During the charging process, the voltage gradually increases and sodium ions are removed from the cathode material. The slope and smooth region of the voltage curve can reflect the phase transition behavior and electrochemical reversibility of the material. During the discharge process, the voltage gradually decreases and the sodium ions are embedded in the cathode material. The shape of the discharge curve can reflect the ion diffusion kinetics of the material and the reversibility of the electrode reaction. The results show that Na^+ has a good diffusion ability in the NFM electrode, and its main diffusion coefficient ranges from 10-15 cm2 s^{-1} to 10-12 cm2 s^{-1}. In conclusion, Na^+ has excellent diffusion performance in the electrode, and the ion diffusion ability of the material is gradually stabilized with the gradual increase of the cycling time, which indicates that the material possesses a better long-cycling performance. It can be seen that the ultra-small particle size synthesized by microwave-assisted synthesis shortens the diffusion path, which is conducive to the fastest diffusion kinetics of sodium ions, which is manifested in the excellent electrochemistry.

4. Conclusions

In summary, NFM materials with tunable particle size were synthesized by microwave-assisted synthesis. Notably, the W-NFM-10 sample exhibited excellent electrochemical performance, providing a specific capacity of 83.5 mAh/g at 0.1C magnification, and maintaining a specific capacity of 36.37 mAh/g even at a high magnification of 5C. After 150 cycles at 1C magnification in the cycling test, the specific capacity remained 88.67 mAh/g, a capacity retention rate of 91.80%. The excellent performance in the comparison can be attributed to the microwave-assisted synthesis of ultra-small particle size, which effectively relieves the bulk stress, enhances the electronic conductivity, and shortens the ion/electron transport path inside the material. Faster and more stable electrochemical reaction kinetics were promoted. This work validates the effectiveness of microwave-assisted synthesis as well as the controlled variable method for enhancing the sodium storage performance of layered cathode materials, and also refines the synthesis process for hydrothermal synthesis of layered electrode materials.

References

[1] Ye Y. Analysis of the Dynamic Influence of New Energy Automobile Market Expansion on Fuel Vehicle Market Share [J]. Advances in Economics, Management and Political Sciences, 2024, 137: 29-33.
[2] Yu X, Wang B, Wang W, et al. Analysis of renewable resources in Central China under the “double carbon” strategy [J]. Energy Reports, 2022, 8: 361-373.
[3] Du K, Xie J, Khandelwal M, et al. Utilization methods and practice of abandoned mines and related rock mechanics under the ecological and double carbon strategy in China-a comprehensive review [J]. Minerals, 2022, 12(9): 1065.
[4] Zhang S, Steubing B, Potter H K, et al. Future climate impacts of sodium-ion batteries [J]. Resources, Conservation and Recycling, 2024, 202: 107362.
[5] Tarascon J M. Na-ion versus Li-ion batteries: complementarity rather than competitiveness [J]. Joule, 2020, 4(8): 1616-1620.
[6] Delmas C. Sodium and sodium-ion batteries: 50 years of research [J]. Advanced Energy Materials, 2018, 8(17): 1703137.
[7] Yabuuchi N, Kubota K, Dahbi M, et al. Research development on sodium-ion batteries [J]. Chemical reviews, 2014, 114(23): 11636-11682.
[8] Wang M, Wang Q, Ding X, et al. The prospect and challenges of sodium-ion batteries for low-temperature conditions [J]. Interdisciplinary Materials, 2022, 1(3): 373-395.
[9] Gao Y, Zhang H, Peng J, et al. A 30-year overview of sodium-ion batteries [J]. Carbon Energy, 2024, 6(6): e464.
[10] G. N. Lewis, C. A. Kraus, J. Am. Chem. Soc. 1910, 32, 1459.
[11] Iwan A, Bogdanowicz K A, Pich R, et al. The Safety Engineering of Sodium-Ion Batteries Used as an Energy Storage System for the Military [J]. Energies, 2025, 18(4): 978.
[12] Zhao Y, Kang Y, Wozny J, et al. Recycling of sodium-ion batteries [J]. Nature reviews materials, 2023, 8(9): 623-634.
[13] Yang Y, Wang Q, Hou J, et al. Enhancing Reversibility and Kinetics of Anionic Redox in O3-NaLi1/3Mn2/3O2 through Controlled P2 Intergrowth [J]. Angewandte Chemie, 2024, 136(43): e202411059.
[14] Li Y, Liu G, Che J, et al. Review on layered oxide cathodes for sodium-ion batteries: Degradation mechanisms, modification strategies, and applications [J]. Interdisciplinary Materials, 2025, 4(1): 24-51.
[15] Huang Y, Zhang Y, Yuan G, et al. Multi-element doped hexagonal sheet Ni/Mn-based layered oxide with ZrO_2 surface modification for sodium ion batteries cathode with high capacity and good cycle/air stability [J]. Applied Surface Science, 2024, 653: 159395.
[16] Lewis G N, Kraus C A. The Potential of the Sodium Electrode [J]. Journal of the American Chemical Society, 1910, 32(11): 1459-1468.
[17] Gao H, Zeng J, Sun Z, et al. Advances in layered transition metal oxide cathodes for sodium-ion batteries [J]. Materials Today Energy, 2024: 101551.

[18] Wang Y, Jin J, Zhao X, et al. Unexpected Elevated Working Voltage by Na^+/Vacancy Ordering and Stabilized Sodium-Ion Storage by Transition-Metal Honeycomb Ordering [J]. Angewandte Chemie, 2024, 136(38): e202409152.
[19] Zhang T, Ji H, Hou X, et al. Promoting the performances of P2-type sodium layered cathode by inducing Na site rearrangement [J]. Nano Energy, 2022, 100: 107482.
[20] Liu Y F, Han K, Peng D N, et al. Layered oxide cathodes for sodium-ion batteries: from air stability, interface chemistry to PHase transition [J]. InfoMat, 2023, 5(6): e12422.
[21] Lim S G, Kwon M S, Kim T, et al. Correlation between the cation disorders of Fe^{3+} and Li^+ in P3-type $Na_{0.67}[Li_{0.1}(Fe_{0.5}Mn_{0.5})_{0.9}]O_2$ for sodium ion batteries [J]. ACS Applied Materials & Interfaces, 2022, 14(29): 33120-33129.
[22] Wang Q C, Shadike Z, Li X L, et al. Tuning sodium occupancy sites in P2-layered cathode material for enhancing electrochemical performance [J]. Advanced Energy Materials, 2021, 11(13): 2003455.
[23] Song T, Chen L, Gastol D, et al. High-voltage stabilization of O3-type layered oxide for sodium-ion batteries by simultaneous tin dual modification [J]. Chemistry of Materials, 2022, 34(9): 4153-4165.
[24] Wang C, Liu L, Zhao S, et al. Tuning local chemistry of P2 layered-oxide cathode for high energy and long cycles of sodium-ion battery [J]. Nature communications, 2021, 12(1): 2256.
[25] Gayara R A H, Moossa B, Shakoor R A, et al. Cost-effective microwave-assisted O3-type sodium-based layered oxide cathode materials for sodium-ion batteries [J]. Energy Reports, 2023, 10: 837-849.
[26] Li Z, Peng K, Ji N, et al. Advanced mechanisms and applications of microwave-assisted synthesis of carbon-based materials: a brief review [J]. Nanoscale Advances, 2025.
[27] Pawelski, Damian, and Marta E. Plonska-Brzezinska. "Microwave-assisted synthesis as a promising tool for the preparation of materials containing defective carbon nanostructures: implications on properties and applications." Materials 16.19 (2023): 6549.
[28] SHALOM, PAULCY RANI PR, et al. "Microwave assisted synthesis of $NiMn_2O_4$ as electrode material for supercapacitor applications." Zastita Materijala 65.3 (2024): 501-509.
[29] Konwar, Madhabi, and Lakhya Jyoti Borthakur. "Synergistic effect of SGO/Nickel cobalt sulfide nanocomposite on Ni-foam for supercapacitor performance with widened potential windows− A microwave-assisted synthesis." Journal of Industrial and Engineering Chemistry 145 (2025): 419-429.
[30] Gerard, Ong, et al. "Fabrication of binder-free nickel-manganese PHosPHate battery-type electrode by microwave-assisted hydrothermal technique." Journal of Alloys and Compounds 941 (2023): 168878.
[31] Chen, Yifan, et al. "Microwave-assisted synthesis of highly uniform Prussian Blue@ Carbon cathode materials for sodium-ion batteries." Journal of Power Sources 615 (2024): 235085.
[32] ARACHCHIGE, HARINDI G. RANASINGHE. "MICROWAVE-ASSISTED SOL-GEL SYNTHESIS OF SODIUM-BASED LAYERED OXIDE CATHODE MATERIALS FOR HIGH-PERFORMANCE SODIUM-ION BATTERIES." (2023).
[33] Han, Gang, et al. "Study of microwave non-thermal effects on hydrogen bonding in water by Raman spectroscopy." Spectrochimica Acta Part A: Molecular and Biomolecular Spectroscopy 285 (2023): 121877.
[34] Gholipour, Arsalan, and Shahrzad Rahmani. "The synthesis of fluorescent carbon quantum dots for tartrazine detection in food: a novel one-step microwave heating approach." Fullerenes, Nanotubes and Carbon Nanostructures 31.8 (2023): 743-751
[35] F. Liao, X. Han, Y. Zhang, C. Xu, H. Chen (2018) Ceramics International 44: 22622-22631.
[36] T. H. Dolla, K. Pruessner, D. G. Billing, C. Sheppard, A. Prinsloo, E. Carleschi et al (2018) Journal of Alloys and Compounds 742: 78-89.
[37] P. Butreddy, H. Holden, H. Rathnayake (2022) Macromol, Chem. PHys 223: 2200237-2200243.